Efficient silicon solar cells with dopant-free asymmetric heterocontacts

James Bullock[1,2,3,4], Mark Hettick[1,2,3], Jonas Geissbühler[5], Alison J. Ong[1,2,3], Thomas Allen[4], Carolin M. Sutter-Fella[1,2,3], Teresa Chen[6], Hiroki Ota[1,2,3], Ethan W. Schaler[1], Stefaan De Wolf[5], Christophe Ballif[5], Andrés Cuevas[4] and Ali Javey[1,2,3]*

A salient characteristic of solar cells is their ability to subject photo-generated electrons and holes to pathways of asymmetrical conductivity—'assisting' them towards their respective contacts. All commercially available crystalline silicon (c-Si) solar cells achieve this by making use of doping in either near-surface regions or overlying silicon-based films. Despite being commonplace, this approach is hindered by several optoelectronic losses and technological limitations specific to doped silicon. A progressive approach to circumvent these issues involves the replacement of doped-silicon contacts with alternative materials which can also form 'carrier-selective' interfaces on c-Si. Here we successfully develop and implement dopant-free electron and hole carrier-selective heterocontacts using alkali metal fluorides and metal oxides, respectively, in combination with passivating intrinsic amorphous silicon interlayers, resulting in power conversion efficiencies approaching 20%. Furthermore, the simplified architectures inherent to this approach allow cell fabrication in only seven low-temperature (≤200 °C), lithography-free steps. This is a marked improvement on conventional doped-silicon high-efficiency processes, and highlights potential improvements on both sides of the cost-to-performance ratio for c-Si photovoltaics.

The majority of c-Si solar cells within both industry and research laboratories make use of doped homojunctions to separate photo-generated electrons and holes. Researchers tasked with optimizing these doped homojunctions are faced with a myriad of interrelated optical, carrier transport and recombination based losses, most notably parasitic absorption[1], Auger recombination and other heavy doping effects[2,3] (for details see Supplementary Table 1). In addition, technological complexities associated with doping, such as high processing temperatures (>800 °C, with a concomitant necessity for cleanliness), small contact fractions (<0.5%), dopant glass removal and junction isolation must be considered[4,5]. These issues can be partially alleviated by switching to architectures which instead use a set of asymmetric carrier-selective heterocontacts—a strategy that has long been considered a crucial technological step to attaining the intrinsic efficiency limit of c-Si (ref. 6). Carrier-selective heterocontacts provide a negligible resistance to the collected carrier (synonymous with a low contact resistivity) whilst simultaneously 'blocking' the other carrier (equivalent to low contact recombination). This can be achieved through a number of possible mechanisms at the heterocontact—for example using surface passivating layers or stacks which provide conductivity asymmetry through band offsets, tunnelling probabilities or band bending when applied to c-Si (ref. 7).

In recent years, the benefits of the asymmetric heterocontact concept have been realized, perhaps most famously by the silicon heterojunction cell architecture (SHJ, sometimes called HIT,

'heterojunction with intrinsic thin layer'), which has now overtaken its homojunction counterpart in terms of efficiency, claiming the world record for c-Si in 2014 (ref. 8). Nonetheless, thus far, all competitive demonstrations of asymmetric heterocontacts[9–11], including the SHJ technology, still rely on doped-silicon layers, which introduce complex deposition optimizations and parasitic optical losses[12–14]. A further advancement of the asymmetric carrier-selective heterocontact concept is to completely replace doped-silicon layers with alternative materials which do not incur the same fundamental limitations and practical difficulties, as has been realized on amorphous silicon absorber cells previously[15]. Several such carrier-selective materials have now been demonstrated on c-Si, including transition metal oxides[16–19], organic films[20–22] and metal–insulator structures (used in metal–insulator–semiconductor inversion layer solar cells)[23–25], many of which were previously implemented in other absorber-type solar cells[15,26–28]. In contrast to the limitations of doped-silicon regions and layers, the use of different carrier-selective materials opens a wider optical and electrical parameter space, decoupling the optimization of different solar cell components. Furthermore, they can generally be deposited using simpler techniques (evaporation, spin coating, spray pyrolysis and so on), at low temperatures—potentially reducing the cost and complexity of fabrication. Nevertheless, as it stands, c-Si solar cells implementing a set of dopant-free asymmetric heterocontacts (DASH cells) have been limited to efficiencies less than 14% (refs 29–32), hindered mostly by carrier recombination losses at the heterointerface with c-Si. This paper demonstrates a

---

[1]Department of Electrical Engineering and Computer Sciences, University of California, Berkeley, California 94720, USA. [2]Berkeley Sensor and Actuator Center, University of California, Berkeley, California 94720, USA. [3]Materials Sciences Division, Lawrence Berkeley National Laboratory, Berkeley, California 94720, USA. [4]Research School of Engineering, The Australian National University (ANU), Canberra, Australian Capital Territory 0200, Australia. [5]École Polytechnique Fédérale de Lausanne (EPFL), Institute of Micro Engineering (IMT), Photovoltaics and Thin Film Electronic Laboratory (PVLab), Maladière 71b, CH-200 Neuchatel, Switzerland. [6]The Molecular Foundry, Lawrence Berkeley National Laboratory, Berkeley, California 94720, USA. *e-mail: ajavey@eecs.berkeley.edu
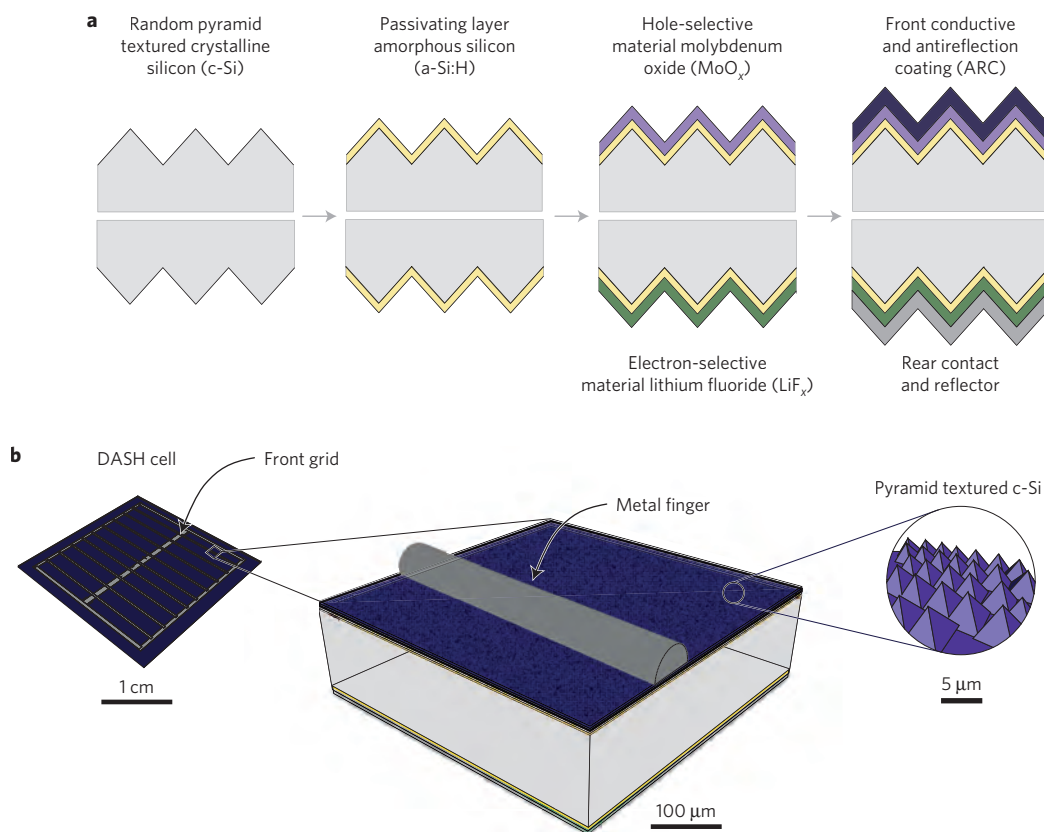
Figure 1 | Conceptual structure of the DASH solar cell. a, Cross-section of the DASH cell structure showing the incremental addition of layers. Of notable benefit is the inherent simplicity of the approach, requiring no lithography or high-temperature processing. **b**, 3D representation showing the metal grid and texture of the front (sunward) side of the DASH cell.

marked improvement on the state-of-the-art DASH cell, facilitated by dopant-free heterocontacts which implement thin passivating interlayers, the electron contact of which is presented for the first time here. By addressing surface recombination using passivating interlayers, proof-of-concept cells with open-circuit voltages in excess of 700 mV and conversion efficiencies close to 20% have been demonstrated. These developments promote the DASH cell approach into the realm of competitive c-Si cell architectures.

DASH cell concept

Figure 1 outlines the conceptual structure of the DASH c-Si solar cell explored in this work. In this instance, as in the SHJ cell, thin passivating intrinsic hydrogenated amorphous silicon a-Si:H(i) films are implemented on both sides of the wafer. Unlike doped a-Si:H films, which result in 100% parasitic absorption, these less-defective intrinsic thin films contribute some current to the solar cell[12]. More importantly these layers greatly reduce the carrier recombination rate at the c-Si surface, enabling a high excess carrier concentration under illumination, essential for a high solar cell operating voltage. Such layers must be kept sufficiently thin to avoid excessive resistance and absorption losses[12]. We note these a-Si:H(i) films are not integral to the DASH concept and could be replaced in the future with other non-absorbing or higher-lifetime organic or inorganic passivating films. On top of the thin passivating layer electron-selective and hole-selective materials are deposited on opposite wafer surfaces. In contrast to the SHJ process, rather than using doped a-Si:H films, in this study transparent materials with extreme work-function values are chosen to achieve carrier selectivity. Ideally, when a material with a very low work function is applied to lightly doped c-Si, accumulation of electrons (and repulsion of holes) occurs near the surface. This

high concentration of surface electrons reduces the heterocontact resistivity and the corresponding low hole surface concentration reduces the probability of Shockley–Read–Hall recombination at the heterocontact interface. The corollary holds for holes and high-work-function materials. In this manner, by placing materials with an extreme work-function difference on either side of a c-Si wafer, efficient separation of photo-generated carriers can be achieved. Finally, the remaining supporting structures (transparent conductive oxide and metal contacts) are deposited—enabling optimal light coupling into the cell and low resistive losses for photo-generated carriers en route to the external circuit.

Central to the DASH cell concept is the functionality of the carrier-selective heterocontacts. For the hole-selective side, we previously developed an a-Si:H(i)/molybdenum oxide MoO_x-based contact to c-Si which owes its hole selectivity to the very large work function of MoO_x (refs 17,33). Such a structure has recently been demonstrated to be compatible with efficiencies above 22% (ref. 34). However, a dopant-free electron-selective heterocontact with an equivalent level of performance has yet to be demonstrated. A group of proven electron-selective materials, frequently used in organic devices, is that formed by the alkali and alkaline earth metal salts. These materials consist of a metal cation from groups 1 or 2 of the periodic table ionically bonded to different anions, such as carbonate[35], acetate[36] or halogens[36–38]. Although there still exists some contention as to the mechanism of the high electron conductivity across this interface[35–37], most studies attribute the formation of a low-work-function electrode as the most important consequence. Of particular interest within this group of materials are the alkali metal fluorides (AMFs). Thermally evaporated AMFs are explored here as a novel component, complementary to MoO_x, for c-Si solar cells. Such a combination has been implemented on
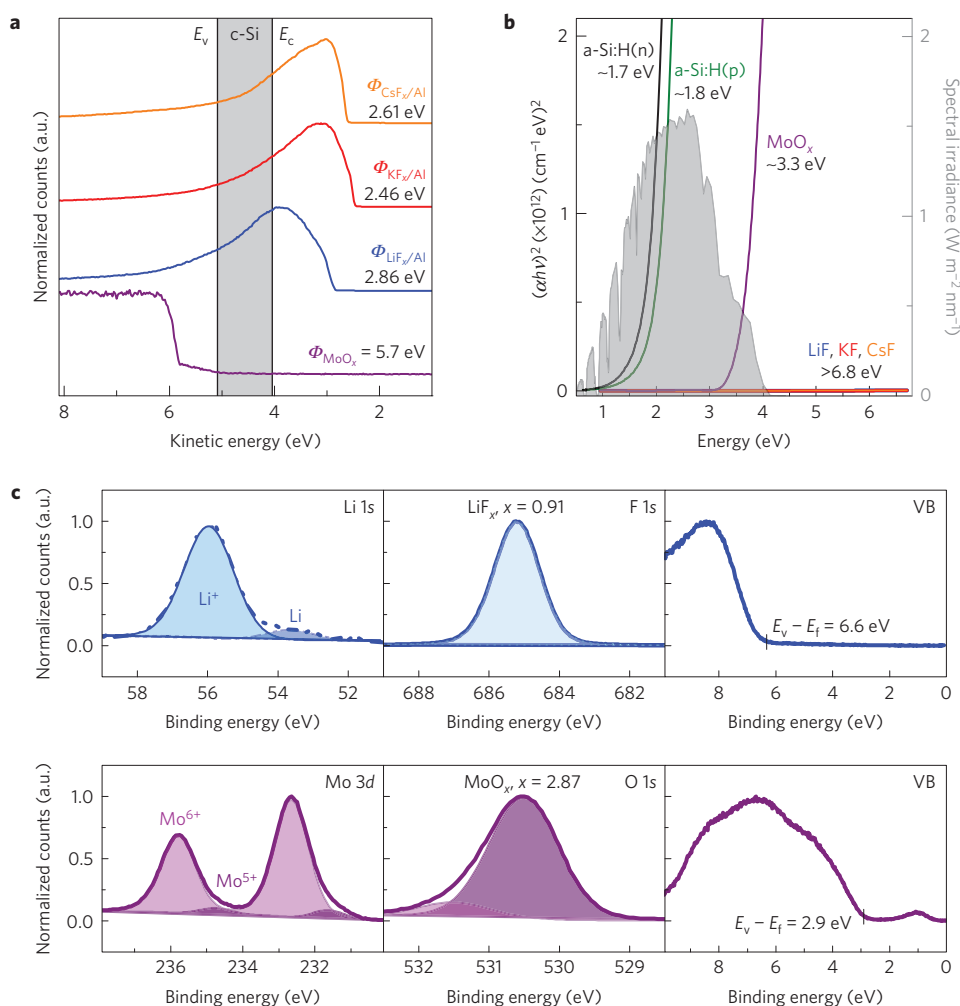
Figure 2 | Optoelectronic properties of carrier-selective layers. a, Secondary electron cutoff spectrum yielding low work function values Φ for electron-selective contacts measured at the LiF$_x$/Al, KF$_x$/Al and CsF$_x$/Al interfaces. A spectrum for the high-work-function hole-selective material MoO$_x$, developed previously, is also included. The shaded area represents the band position of c-Si. **b**, Tauc plot of carrier-selective materials LiF$_x$, KF$_x$, CsF$_x$ and MoO$_x$. As a reference the AM 1.5G spectrum (which represents the Sun's irradiance on Earth) is included. These are compared with the highly absorbing phosphorus and boron-doped a-Si:H films used in SHJ cells. **c**, Core level and valence band spectra for LiF$_x$ and MoO$_x$ films, fitted with multiple Voigt peaks (shaded areas) to quantify the contribution of different oxidation states. The estimated stoichiometry of the two materials of the two films is also included.

other absorber materials previously. Three representative AMFs (LiF$_x$, KF$_x$ and CsF$_x$) are studied to identify which presents the best contact properties to c-Si.

Optoelectronic properties of carrier-selective materials

As discussed above, the work function of the carrier-selective materials can play a crucial role in the efficacy of the DASH cell approach. The X-ray photoelectron spectroscopy (XPS) secondary electron cutoff analysis presented in Fig. 2a shows very low work-function values of the LiF$_x$/Al, KF$_x$/Al and CsF$_x$/Al interfaces, measured to be 2.86, 2.46 and 2.61 eV, respectively. Provided in the same plot is the previously measured value of ∼5.7 eV for the high-work-function material MoO$_x$ (ref. 17), demonstrating the desired extreme work-function separation as discussed above.

A unique advantage of dopant-free heterocontacts is the ability to separately tune their optical and electronic impact on the solar cell. A Tauc plot for LiF$_x$, KF$_x$, CsF$_x$ and MoO$_x$ films is provided in Fig. 2b, alongside the AM 1.5G spectrum, to evaluate the significance of their absorption. Also included in this Tauc plot are trends for phosphorus- and boron-doped a-Si:H, which are typically implemented as ∼10 nm films in standard doped-silicon SHJ cells[39].

It can be seen that the MoO$_x$ and AMF films exhibit higher transparency across the spectrum than the conventional doped a-Si:H layers. The Tauc energy gap E_{Tauc} of the AMFs is greater than the measurement range (>6.8 eV), resulting in negligible absorption, whereas MoO$_x$ films exhibit an E_{tauc} of ∼3.3 eV, resulting in minor absorption of high-energy light (where the Sun's irradiance is relatively low). Ray tracing simulations reveal that compared to the SHJ cell's doped-silicon heterocontacts, a reduction in front-film parasitic absorption of ∼1 mA cm^{-2} could be achieved by switching to an optimized dopant-free heterocontact cell design (see Supplementary Note 1 and Fig. 1). In addition, core level and valence band XPS analyses of LiF$_x$ and MoO$_x$ films are shown in Fig. 2c. The valence band of the LiF$_x$ is measured to be ∼6.6 eV from the Fermi energy and shows no clear sub-band features despite the reduced component suggested by the shape of the Li 1s peaks. The MoO$_x$ valence band and core levels are in alignment with those previously measured for evaporated films, showing the clear formation of a sub-band peak originating from a reduced MoO$_x$ state that has demonstrated importance for its carrier-selective function[17]. Extractions of the film stoichiometry based on core level peak areas also support a slightly reduced cation oxidation state for both LiF$_x$ and MoO$_x$ films.
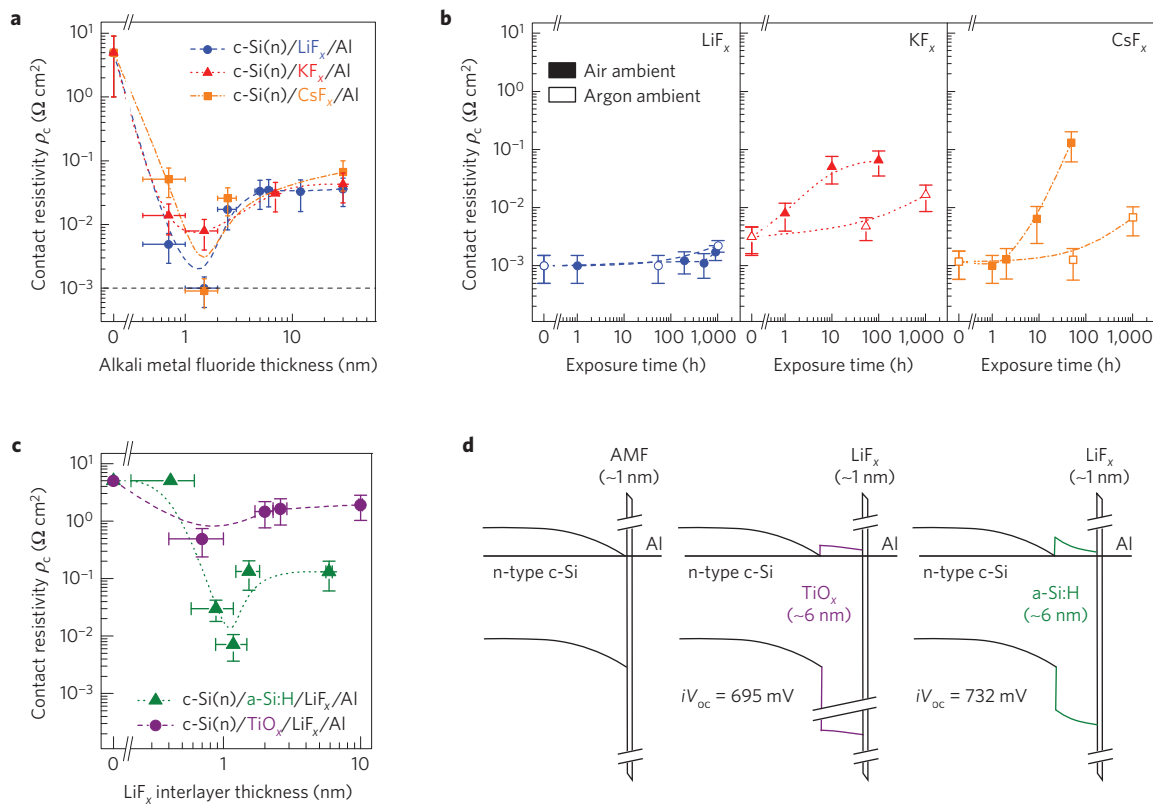
Figure 3 | Contact-level analysis of electron-selective contacts. a,b, Contact resistivity of LiF_x/Al (blue), KF_x/Al (red) and CsF_x/Al (orange) contacts made to n-type silicon as a function of the AMF interlayer thickness (**a**) and exposure time to air (filled) and argon (open) ambient (**b**). The dotted horizontal line in **a** represents the estimated resolution of the ρ_c extraction technique (see Supplementary Note 2). **c**, Evolution of ρ_c against LiF_x thickness for heterocontacts with TiO_x (purple) and a-Si:H(i) (green) interlayers. **d**, Schematics of the direct AMF/Al contact as well as heterocontacts implementing TiO_x and a-Si:H(i) interlayers. The implied open-circuit voltages iV_{oc} of the two passivating layers are also included. Error bars are based on the measured spread in data or estimated error in the measurement (whichever is largest). Lines provide a guide to the eyes only.

Electron heterocontact development

Whereas the electrical contact properties of MoO_x-based hole-selective heterocontacts on c-Si have previously been characterized and shown to be promising for c-Si solar cells[17–19,33,34,40], the application of AMF/Al electron-selective contacts in c-Si solar cells remains relatively unexplored[32,41]. Figure 3a shows that the contact resistivity ρ_c for LiF_x/Al (blue), KF_x/Al (red) and CsF_x/Al (orange) to moderately doped n-type ($N_d \sim 5 \times 10^{15}$ cm^{-3}) c-Si has a strong dependence on the AMF interlayer thickness, with all three materials producing the lowest ρ_c values in the 0.5–1.5 nm range. The lowest extracted values of $\sim$1 mΩ cm^2 for the LiF_x/Al and CsF_x/Al contacts are at the limit of the measurement resolution, representing an upper limit ρ_c (for details see Supplementary Note 2). Such values are exceptionally low, given the well-known difficulties of contacting moderate resistivity n-type c-Si—an issue associated with Fermi level pinning and the position of silicon's charge neutrality level close to the valence band[42]. This introduces the possibility of previously unattainable cell architectures—for example, n-type undiffused partial rear contact cells. The measured stability of these electron-selective contacts in both air (filled markers) and argon (open markers) is provided in Fig. 3b. An increase in ρ_c for CsF_x-based and KF_x-based contacts is seen within the first 24 h of air exposure. This increase is slowed by more than an order of magnitude as a result of storing the samples in argon ambient. The LiF_x electron-selective contact, however, exhibits exceptional longevity, with negligible degradation over 1,000 h in both environments, and is therefore used in the DASH cells presented in this work.

A high rate of recombination at the c-Si/LiF_x interface precludes the direct implementation of full-area LiF_x/Al electron-selective contacts into solar cells (for details see Supplementary Note 2). This issue can be amended by the addition of a thin passivating interlayer between the c-Si and LiF_x/Al stack. As shown in Fig. 3d, two potential candidates for passivating the c-Si surface are hydrogenated amorphous silicon a-Si:H(i) (as used in the SHJ cell) and titanium oxide TiO_x (refs 16,30). Both of these films greatly reduce the c-Si surface recombination rate, allowing a high implied open-circuit voltage V_{oc} around 700 mV, in line with state-of-the-art surface passivation (for details see Supplementary Note 2). Figure 3c shows the dependence of ρ_c on LiF_x thickness for n-type wafers passivated with $\sim$6 nm TiO_x (purple) or a-Si:H(i) (green) films. Clear improvements in electron selectivity seen with the addition of the LiF_x/Al contact for these disparate passivation strategies highlight the versatility of this approach. Optimum ρ_c values of 500 and 7 mΩ cm^2 are found for the TiO_x/LiF_x/Al and a-Si:H(i)/LiF_x/Al heterocontacts, respectively, both with a LiF_x interlayer thickness of $\sim$1 nm. These two values fall at the upper and lower ends of an equivalent ρ_c range reported in the literature for doped-silicon-based heterocontacts[43,44]. Simulating these contacts within an idealized solar cell indicates that both systems could be effectively applied as full-area electron heterocontacts and that devices implementing a-Si:H(i) interlayers will produce higher efficiencies (for details see Supplementary Note 3 and Supplementary Fig. 4).

High-efficiency proof-of-concept DASH cells

Finally, high-efficiency DASH cells implementing a-Si:H(i)/LiF_x/Al and a-Si:H(i)/MoO_x heterocontacts were fabricated. Cross-sectional scanning electron micrographs of the top and bottom random pyramidal textured surfaces of the DASH cell are included in Fig. 4a.
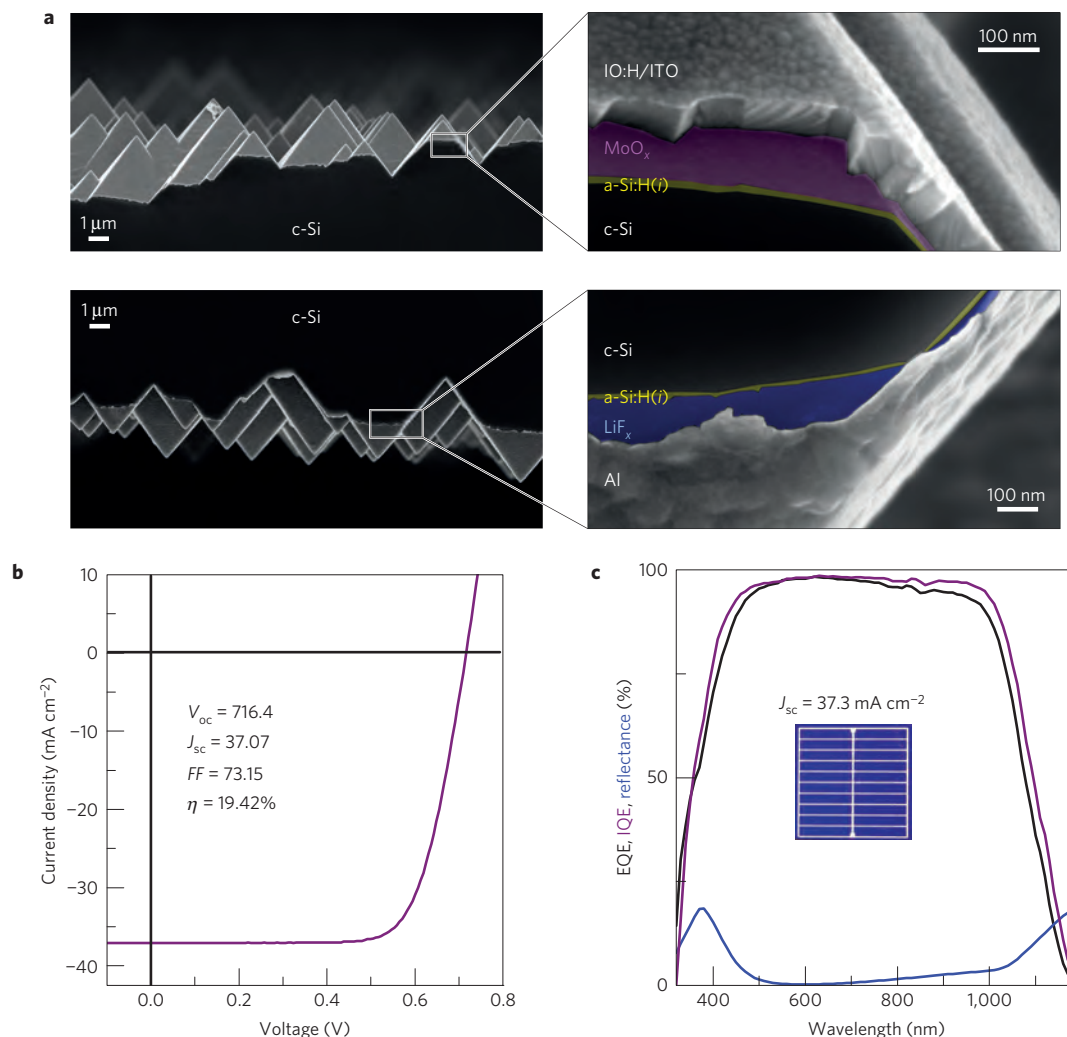
Figure 4 | DASH cell level results. a, Cross-sectional scanning electron micrographs of the textured front (top images) and back surfaces (bottom images) of the DASH cell. The expanded views on the right are false coloured to highlight the different films on each surface. Scale bars, 1 μm (left); 100 nm (right). **b**, Light J–V behaviour and cell characteristics of the DASH cell measured under standard 1 sun conditions. **c**, External (black) and internal (purple) quantum efficiencies alongside the measured reflectance (blue) for the DASH cells. The J_{sc} obtained from the external quantum efficiency, shown above a photograph of the DASH cell, agrees well with that measured from the light J–V analysis.

Texturing is employed to enhance both the amount of light coupled into the cell and the path length of that light once inside the cell. Of notable benefit in this cell architecture is the fabrication procedure, requiring just seven low-temperature steps without the use of complex alignment or photolithography. This offers a significant simplification over dopant-diffused high-efficiency architectures, which involve ~20 steps and a high thermal budget[45]. The simple, room-temperature deposition of dopant-free selective layers also potentially introduces benefits over doped a-Si:H layers, used in SHJ cells, which are typically deposited at ~200 °C using toxic gases and require precise condition control to balance trade-offs between J_{sc}, V_{oc} and fill factor based losses[12–14].

Light J–V measurements provided in Fig. 4b show that power conversion efficiencies η of up to 19.4% have been achieved in the early stages of this DASH cell development, enabled by V_{oc}, J_{sc} and fill factor values of 716 mV, 37.07 mA cm^{-2} and 73.15%, respectively. The statistics of the champion cell batch reveal a tight spread in results, with an average efficiency above 19%, a testament to the reproducibility of this DASH cell design (see Supplementary Table 2). An accompanying spectral response analysis, shown in Fig. 4c, reveals a high quantum collection efficiency over most of the AM1.5G spectrum (see Supplementary Fig. 5 and Supplementary

Note 4 for further DASH cell characterization). An enhancement in the rear-side reflection and a reduction in the series resistance of the DASH cell are identified as the two most likely paths towards higher efficiency for this design. An improvement in J_{sc} of ~1 mA cm^{-2} could arise by replacing Al with Ag (or possibly ITO), and a boost in the fill factor above 79% could occur by further reducing the resistive loses, as detailed in the Supplementary Note 4. It is envisaged that future iterations of this DASH approach could be combined with even lower thermal budget processing—integrating amorphous transparent conductive oxides[46,47], plating metalliza-tion[34] and low-cost, low-temperature back-end processing[48].

Conclusions

In this work we have demonstrated the DASH cell concept—a simple, low-temperature c-Si solar cell featuring dopant-free heterocontacts—with high power conversion efficiency. A key enabling factor is the development of a novel c-Si/a-Si:H(i)/LiF$_x$/Al electron-selective heterocontact to complement the recently developed a-Si:H(i)/MoO$_x$ hole-selective heterocontact. Proof-of-concept device efficiencies approaching 20% have been achieved, supported by a high V_{oc} and low contact resistance at both heterocontacts. This represents a significant improvement on

the state of the art for this approach (from η of ~14 to ~20%), bringing the DASH architecture into the competitive realm of industrially applicable technologies, including doped-silicon SHJ and conventional dopant-diffused architectures. The versatility and simplicity of the DASH approach can also potentially benefit more advanced solar cell architectures. In particular, dopant-free interdigitated back contact or dopant-free bifacial (using, for example, LiF$_x$/transparent conductive oxide contacts) solar cells are both logical extensions of this work. The advancement past the limitations of single-junction c-Si cells could also be facilitated using dopant-free carrier-selective contacts for a c-Si bottom cell in a monolithic tandem-cell structure. Put simply, the above-developed DASH system can effectively be viewed as a toolbox for a wide range of c-Si solar cell architectures, providing opportunities for facile fabrication of high-efficiency device structures at low temperatures.

Methods

Carrier-selective materials (LiF$_x$, KF$_x$, CsF$_x$, MoO$_x$) used in this study were deposited by vacuum thermal evaporation from powder sources (>3 N purity). Controlled deposition rates of 0.25–1 Å s^{-1} (as monitored by a crystal oscillator) were used at a base pressure of <5 × 10^{-6} mbar.

Materials characterization. For XPS characterization, thin films of LiF$_x$, KF$_x$, CsF$_x$, MoO$_x$ or Al (or combinations thereof) were deposited on polished c-Si wafers. A Kratos AXIS Ultra DLD system with a monochromatic Al Kα X-ray source and a hemispherical analyser was used for the measurements. Secondary electron cutoff and valence band measurements were performed using X-ray excitation, with an added bias to extract the cutoff edge. Linear fits from the respective edges were used to extract numerical values for $E_f - E_v$ (at the valence band edge) and the work functions of the AMF/Al interfaces. For the valence band measurements, thin layers of the final implemented contact materials (MoO$_x$ and LiF$_x$) were characterized directly on as-evaporated c-Si substrates to reveal the electronic structure near the valence band edge. Work functions were extracted from evaporated AMF/Al bilayers, with the Al thinned down to <5 nm by Ar ion milling (4 kV) *in situ* to observe the work-function modification of the Al contact overlayer by the different AMFs. A Au reference work function at 5.2 eV was measured in the same measurement session, confirming the accuracy of measurements. The core level spectra were fitted using the commonly applied Voigtian peak shapes and Shirley background correction to extract the stoichiometry of the contact layers by the ratio of scaled peak areas. Peak areas were extracted from the background corrected Voigt fits of Li 1s, F 1s, Mo 3d and O 1s spectra presented in Fig. 2, and scaled by their relative atomic sensitivity factors[49] (normalized to F 1s). As expected, owing to the decomposition of these materials during the evaporation process, the MoO$_x$ contact layer achieves a value of x approximately 2.87 (after accounting for the carbon-related oxygen contaminant peak commonly seen in O 1s levels for MoO$_x$ films[50]), and the LiF$_x$ contact layer is measured to have an x value of approximately 0.91, representing slightly sub-stoichiometric films in both cases. For the LiF$_x$ material, a sub-stoichiometric film is observed due to the presence of a reduced Li(0) peak, also observed in previous XPS measurements on LiF$_x$ (ref. 51). The MoO$_x$ Mo 3d level indicates both the 6$^+$ and 5$^+$ oxidation states as in previous explorations of evaporated films[17], a feature attributed to the formation of a defect band in as-evaporated MoO$_x$ films.

Absorbance measurements were performed on transparent substrates with thin films of LiF$_x$, KF$_x$, CsF$_x$ and MoO$_x$ on one side (CaF$_2$ substrates were used for the AMFs and quartz was used for the MoO$_x$). Measurements were taken using a N$_2$-purged spectrophotometer (Cary 5000 UV–Vis–NIR spectrophotometer).

Contact structure and measurement. The c-Si(n)/AMF/Al electron-selective contacts were fabricated on planar, n-type (N_d ~ 5 × 10^{15} cm^{-3}), float zone (FZ), c-Si wafers with a thickness of ~200 μm. These were subjected to a dilute HF dip before evaporation of the contact structures. A full-area stack consisting of ~1.5 nm of AMF and ~250 nm of Al was evaporated on the rear side of the contact structures without breaking vacuum. An array of different diameter circles was evaporated on the front of the test structures by means of a shadow mask. These circles were deposited as a stack of variable thicknesses of AMF capped with ~250 nm of Al, and ρ_c was extracted as described in Supplementary Note 2 and Supplementary Fig. 2.

For the interlayer contact study, hydrogenated amorphous silicon films of ~6 nm were deposited by means of plasma-enhanced chemical vapour deposition (PECVD) at ~200 °C on pyramidal textured, FZ, n-type (N_d ~ 1 × 10^{15} cm^{-3}) c-Si wafers. Titanium oxide films of ~6 nm were deposited on planar, FZ, n-type

(N_d ~ 5 × 10^{15} cm^{-3}), c-Si wafers by means of atomic layer deposition (ALD) at ~230 °C using alternating pulses of titanium isopropoxide and water (growth rate of ~0.03 nm/cycle). Both sets of samples received standard RCA cleaning and dilute HF dips immediately before deposition (see Supplementary Note 2 and Supplementary Fig. 3 for details on the passivating interlayers). Contact structures were fabricated and ρ_c was extracted as above. The minor difference in doping concentration is not expected to significantly affect the measured ρ_c.

Solar cell structure and measurement. High-efficiency cells (2 × 2 cm^2) were fabricated on double-side pyramidal textured, FZ, n-type (N_d ~ 1 × 10^{15} cm^{-3}) wafers with a thickness of ~240 μm. Following standard RCA cleaning and a dilute HF dip, the cells were passivated on both sides with a ~6 nm intrinsic a-Si:H(i) layer, grown at 200 °C by means of PECVD in an Octopus I reactor from INDEOtec SA. On the front side of the cell, ~10 nm of MoO$_x$ was thermally evaporated, on top of which a bilayer consisting of ~55 nm of hydrogenated indium oxide and ~10 nm of ITO was sputtered (MRC 603) at room temperature through a 2 × 2 cm^2 shadow mask to define the cell area. A screen-printed Ag front grid with a corresponding contact fraction of ~5% was printed and baked at ~130 °C. Following this, on the rear side, an ~1 nm LiF$_x$/~100 nm Al stack was evaporated without breaking vacuum. Cross-sectional scanning electron micrographs were taken on a Zeiss Gemini Ultra-55. Light $J–V$ characteristics were measured under standard 1 sun conditions (AM 1.5G spectrum, 100 mW cm^{-2}, 25 °C) with a Wacom solar simulator, and EQE was measured using an in-house built set-up. No bus bar exclusion was made in the current density measurement for the high-efficiency DASH cells. Peripheral absorption was avoided by using an aperture mask.

References

1. Baker-Finch, S. C., McIntosh, K. R., Yan, D., Fong, K. C. & Kho, T. C. Near-infrared free carrier absorption in heavily doped silicon. *J. Appl. Phys.* **116**, 063106 (2014).
2. Richter, A., Glunz, S. W., Werner, F., Schmidt, J. & Cuevas, A. Improved quantitative description of Auger recombination in crystalline silicon. *Phys. Rev. B* **86**, 165202 (2012).
3. Cuevas, A., Basore, P. A., Giroult-Matlakowski, G. & Dubois, C. Surface recombination velocity of highly doped n-type silicon. *J. Appl. Phys.* **80**, 3370–3375 (1996).
4. Zhao, J., Wang, A., Green, M. A. & Ferrazza, F. 19.8% efficient 'honeycomb' textured multicrystalline and 24.4% monocrystalline silicon solar cells. *Appl. Phys. Lett.* **73**, 1991–1993 (1998).
5. Goodrich, A. *et al.* A wafer-based monocrystalline silicon photovoltaics road map: utilizing known technology improvement opportunities for further reductions in manufacturing costs. *Sol. Energy Mater. Sol. Cells* **114**, 110–135 (2013).
6. Tiedje, T., Yablonovitch, E., Cody, G. D. & Brooks, B. G. Limiting efficiency of silicon solar cells. *IEEE Trans. Electron Devices* **31**, 711–716 (1984).
7. Wurfel, U., Cuevas, A. & Wurfel, P. Charge carrier separation in solar cells. *IEEE J. Photovolt.* **5**, 461–469 (2015).
8. Masuko, K. *et al.* Achievement of more than 25%; conversion efficiency with crystalline silicon heterojunction solar cell. *IEEE J. Photovolt.* **4**, 1433–1435 (2014).
9. Taguchi, M. *et al.* 24.7%; record efficiency HIT solar cell on thin silicon wafer. *IEEE J. Photovolt.* **4**, 96–99 (2014).
10. Heng, J. B. *et al.* >23% high-efficiency tunnel oxide junction bifacial solar cell with electroplated Cu gridlines. *IEEE J. Photovolt.* **5**, 82–86 (2015).
11. Feldmann, F. *et al.* Efficient carrier-selective p- and n-contacts for Si solar cells. *Sol. Energy Mater. Sol. Cells* **131**, 100–104 (2014).
12. Holman, Z. C. *et al.* Current losses at the front of silicon heterojunction solar cells. *IEEE J. Photovolt.* **2**, 7–15 (2012).
13. Fujiwara, H. & Kondo, M. Effects of a-Si:H layer thicknesses on the performance of a-Si:H/c-Si heterojunction solar cells. *J. Appl. Phys.* **101**, 054516 (2007).
14. de Nicolás, S. M., Muñoz, D., Ozanne, A. S., Nguyen, N. & Ribeyron, P. J. *Proc. SiliconPV 2011 Conf. 1st Int. Conf. Cryst. Silicon Photovolt.* Vol. 8, 226–231 (2011).
15. Yang, J.-H., Kang, S. J., Hong, Y. & Lim, K. S. Doping-free intrinsic amorphous silicon thin-film solar cell having a simple structure of Glass/SnO$_2$/MoO$_3$/i-a-Si/LiF/Al. *IEEE Electron Device Lett.* **35**, 96–98 (2014).
16. Avasthi, S. *et al.* Hole-blocking titanium-oxide/silicon heterojunction and its application to photovoltaics. *Appl. Phys. Lett.* **102**, 203901 (2013).
17. Battaglia, C. *et al.* Hole selective MoO$_x$ contact for silicon solar cells. *Nano Lett.* **14**, 967–971 (2014).

18. Bullock, J., Cuevas, A., Allen, T. & Battaglia, C. Molybdenum oxide MoO$_x$: a versatile hole contact for silicon solar cells. *Appl. Phys. Lett.* **105**, 232109 (2014).

19. Bivour, M., Temmler, J., Steinkemper, H. & Hermle, M. Molybdenum and tungsten oxide: high work function wide band gap contact materials for hole selective contacts of silicon solar cells. *Sol. Energy Mater. Sol. Cells* **142**, 34–41 (2015).

20. Zielke, D., Pazidis, A., Werner, F. & Schmidt, J. Organic-silicon heterojunction solar cells on n-type silicon wafers: the BackPEDOT concept. *Sol. Energy Mater. Sol. Cells* **131**, 110–116 (2014).

21. Yu, P. *et al.* 13% efficiency hybrid organic/silicon-nanowire heterojunction solar cell via interface engineering. *ACS Nano* **7**, 10780–10787 (2013).

22. Shen, X., Sun, B., Liu, D. & Lee, S.-T. Hybrid heterojunction solar cell based on organic–inorganic silicon nanowire array architecture. *J. Am. Chem. Soc.* **133**, 19408–19415 (2011).

23. Hezel, R. Recent progress in MIS solar cells. *Prog. Photovolt. Res. Appl.* **5**, 109–120 (1997).

24. Ponpon, J. P. & Siffert, P. Open circuit voltage of MIS silicon solar cells. *J. Appl. Phys.* **47**, 3248–3251 (1976).

25. Singh, R., Green, M. A. & Rajkanan, K. Review of conductor–insulator–semiconductor (CIS) solar cells. *Sol. Cells* **3**, 95–148 (1981).

26. Chen, L.-M., Xu, Z., Hong, Z. & Yang, Y. Interface investigation and engineering—achieving high performance polymer photovoltaic devices. *J. Mater. Chem.* **20**, 2575–2598 (2010).

27. Yin, X. *et al.* 19.2% efficient InP heterojunction solar cell with electron-selective TiO$_2$ contact. *ACS Photon.* **1**, 1245–1250 (2014).

28. Zhou, H. *et al.* Interface engineering of highly efficient perovskite solar cells. *Science* **345**, 542–546 (2014).

29. Liu, R., Lee, S.-T. & Sun, B. 13.8% efficiency hybrid Si/organic heterojunction solar cells with MoO$_3$ film as antireflection and inversion induced layer. *Adv. Mater.* **26**, 6007–6012 (2014).

30. Nagamatsu, K. A. *et al.* Titanium dioxide/silicon hole-blocking selective contact to enable double-heterojunction crystalline silicon-based solar cell. *Appl. Phys. Lett.* **106**, 123906 (2015).

31. Zhang, Y. *et al.* High efficiency hybrid PEDOT:PSS/nanostructured silicon Schottky junction solar cells by doping-free rear contact. *Energy Environ. Sci.* **8**, 297–302 (2015).

32. Zhang, Y., Liu, R., Lee, S.-T. & Sun, B. The role of a LiF layer on the performance of poly(3,4-ethylenedioxythiophene):poly(styrenesulfonate)/Si organic-inorganic hybrid solar cells. *Appl. Phys. Lett.* **104**, 083514 (2014).

33. Battaglia, C. *et al.* Silicon heterojunction solar cell with passivated hole selective MoO$_x$ contact. *Appl. Phys. Lett.* **104**, 113902 (2014).

34. Geissbühler, J. *et al.* 22.5% efficient silicon heterojunction solar cell with molybdenum oxide hole collector. *Appl. Phys. Lett.* **107**, 081601 (2015).

35. Li, Y. *et al.* Elucidation of the electron injection mechanism of evaporated cesium carbonate cathode interlayer for organic light-emitting diodes. *Appl. Phys. Lett.* **90**, 012119 (2007).

36. Ganzorig, C., Suga, K. & Fujihira, M. Alkali metal acetates as effective electron injection layers for organic electroluminescent devices. *Mater. Sci. Eng. B* **85**, 140–143 (2001).

37. Helander, M. G., Wang, Z. B., Mordoukhovski, L. & Lu, Z. H. Comparison of Alq3/alkali-metal fluoride/Al cathodes for organic electroluminescent devices. *J. Appl. Phys.* **104**, 094510 (2008).

38. Hung, L. S., Tang, C. W. & Mason, M. G. Enhanced electron injection in organic electroluminescence devices using an Al/LiF electrode. *Appl. Phys. Lett.* **70**, 152–154 (1997).

39. Descoeudres, A. *et al.* >21%; efficient silicon heterojunction solar cells on n- and p-type wafers compared. *IEEE J. Photovolt.* **3**, 83–89 (2013).

40. Bullock, J. *et al.* Proof-of-concept p-type silicon solar cells with molybdenum oxide local rear contacts. *IEEE J. Photovolt.* **5**, 1591–1594 (2015).

41. Kim, S. *et al.* Effects of LiF/Al back electrode on the amorphous/crystalline silicon heterojunction solar cells. *Adv. Mater. Charact. Tech. Sol. Cells* **178**, 660–664 (2013).

42. Schroder, D. K. *Semiconductor Material and Device Characterization* (John Wiley, 2006).

43. Gogolin, R. *et al.* Analysis of series resistance losses in a-Si:H/c-Si heterojunction solar cells. *IEEE J. Photovolt.* **4**, 1169–1176 (2014).

44. Feldmann, F., Bivour, M., Reichel, C., Hermle, M. & Glunz, S. W. Passivated rear contacts for high-efficiency n-type Si solar cells providing high interface passivation quality and excellent transport characteristics. *Sol. Energy Mater. Sol. Cells* **120**, 270–274 (2014).

45. Franklin, E. *et al.* Design, fabrication and characterisation of a 24.4% efficient interdigitated back contact solar cell. *Prog. Photovolt. Res. Appl.* http://dx.doi.org/10.1002/pip.2556 (2014).

46. Demaurex, B. *et al.* Atomic-layer-deposited transparent electrodes for silicon heterojunction solar cells. *IEEE J. Photovolt.* **4**, 1387–1396 (2014).

47. Morales-Masis, M., De Nicolas, S. M., Holovsky, J., De Wolf, S. & Ballif, C. Low-temperature high-mobility amorphous IZO for silicon heterojunction solar cells. *IEEE J. Photovolt.* **5**, 1340–1347 (2015).

48. Dupuis, J. *et al.* Photovoltaic Specialists Conference (PVSC), *2012 38th IEEE 003183–003186* (IEEE, 2012); http://dx.doi.org/10.1109/PVSC.2012.6318254

49. Briggs, D. & Seah, P. *Practical Surface Analysis, Auger and X-ray Photoelectron Spectroscopy* 635–638 (Wiley, 1990).

50. Scanlon, D. O. *et al.* Theoretical and experimental study of the electronic structures of MoO$_3$ and MoO$_2$. *J. Phys. Chem. C* **114**, 4636–4645 (2010).

51. Hamrin, K., Johansson, G., Gelius, U., Nordling, C. & Siegbahn, K. Valence bands and core levels of the isoelectronic series LiF, BeO, BN, and graphite studied by ESCA. *Phys. Scr.* **1**, 277–280 (1970).

Acknowledgements

Author contributions

J.B. and A.J. conceived the idea. J.B. and J.G. carried out the device fabrication, electrical characterization and analysis. A.J.O., T.A. and T.C. assisted with device fabrication. M.H. and C.M.S.-F., assisted with materials characterization. H.O. and E.W.S. assisted with mask fabrication. A.C., S.D.W. and C.B. discussed the results. J.B. wrote the paper and all other authors provided feedback.

Additional information

Supplementary information is available online. Reprints and permissions information is available online at www.nature.com/reprints. Correspondence and requests for materials should be addressed to A.J.

Competing interests

The authors declare no competing financial interests.

Efficient silicon solar cells with dopant-free asymmetric heterocontacts

James Bullock[1,2,3,4], Mark Hettick[1,2,3], Jonas Geissbühler[5], Alison J. Ong[1,2,3], Thomas Allen[4], Carolin M. Sutter-Fella[1,2,3], Teresa Chen[6], Hiroki Ota[1,2,3], Ethan W. Schaler[1], Stefaan De Wolf[5], Christophe Ballif[5], Andrés Cuevas[4] and Ali Javey[1,2,3,*].

[1] Department of Electrical Engineering and Computer Sciences, University of California, Berkeley, California 94720, USA.

[2] Berkeley Sensor and Actuator Center, University of California, Berkeley, California 94720, USA

[3] Materials Sciences Division, Lawrence Berkeley National Laboratory, Berkeley, California 94720, USA.

[4] Research School of Engineering, The Australian National University (ANU), Canberra, ACT 0200, Australia

[5] École Polytechnique Fédérale de Lausanne (EPFL), Institute of Micro Engineering (IMT), Photovoltaics and Thin Film Electronic Laboratory (PVLab), Maladière 71b, CH-200 Neuchatel, Switzerland

[6] The Molecular Foundry, Lawrence Berkeley National Laboratory, Berkeley, California 94720, USA.

*Corresponding author: ajavey@eecs.berkeley.edu

Supplementary Note 1. Optical loss simulations

Modelling of the optical losses was performed using freeware ray tracing software hosted by *PV lighthouse*. The generation current J_g losses of four different solar cell structures were analysed; *i.*) the dopant-free *c*-Si solar cell fabricated in this study, *ii.*) a 'standard' *c*-Si heterojunction solar cell utilising doped-silicon layers,[1] and dopant-free *c*-Si solar cells with improved rear optics by substituting *iii.*) Ag and *iv.*) ITO / Ag for Al. A cell schematic and loss analysis is provided for these four cases in Supplementary Figure 1a. The use of LiF$_x$ interlayers with both Ag and (to a lesser extent) ITO for electron contacts has already demonstrated some promise within the organic electronic community,[2,3] suggesting that they might also be viable contacts on *c*-Si. An improvement of nearly 1 mA/cm^2 in J_{sc} is predicted by using Ag instead of Al. The use of ITO over-layers also introduces the added possibility of bi-facial cells. Optical constants for MoO$_x$ and LiF$_x$ films deposited on polished *c*-Si, are measured using an ellipsometer (using a Cody-Lorentz oscillator model, J. A. Woollam M-2000), and provided in Supplementary Figure 1b. Additional optical constants required for the simulations were sourced from the refractive index library hosted by *PV lighthouse*. It is also worth noting that these simulations assume that 100% of the light absorbed in the *a*-Si:H films is lost to recombination in these films. Whilst this assumption has been found to be true for the doped *a*-Si:H layers, the less defective intrinsic *a*-Si:H layers can still contribute ~30% of their absorbed light to the solar cell current.[4] This suggests the benefits of the DASH approach in terms of reduced parasitic absorption percentage could be even greater than the simulations in Supplementary Figure 1 outline. All simulations do not account for the front-contact shading which can be considered constant (as all cells have the same front ITO sheet resistance they will utilise equivalent front-contact patterns).

Supplementary Note 2. Extraction of the contact resistivity and recombination

Two methods of ρ_c extraction are implemented in this study. The first method, based on the approach introduced by Cox and Strack,[5] involves a series of resistance measurements taken between an array of different diameter front contacts and a full-area rear contact, as shown schematically in Supplementary Figure 2a. The array of different diameter dots was achieved by depositing through a shadow mask. Resistance measurements were taken in the dark at 20 - 25°C using a Keithley 2400 sourcemeter. The resistance versus diameter trend is fitted with a spreading resistance model allowing accurate extraction of ρ_c.[6] The resistance of the measurement setup is also accounted for. An example of this fitting is given in Supplementary Figure 2b. Given the wafer resistivity,

thickness and estimated error in the measurement – the lower limit resolution for this technique is estimated at ~1 mΩcm^2.

The second, simpler but less accurate method, is used to measure devices with ρ_c values > 0.5 Ωcm^2. The resistance between a full-area rear contact and a ~1.1 mm diameter front circular contact was measured and ρ_c was estimated by accounting for the expected bulk spreading resistance. It should be noted in both of the above contact structures that the extracted ρ_c comprises the interfacial resistivities and bulk resistivities of all layers in-between the c-Si and the outer Al layer. Reference samples with only Al contacts (no AMF interlayers) were also fabricated. These contacts exhibited rectifying behaviour when applied both directly and with passivating interlayers (TiO$_x$ and a-Si:H), such that ρ_c was prohibitively high for accurate extraction. In this case a lower limit estimation of ~5 Ωcm^2 is made for these contacts.

The recombination at the direct c-Si(n) / LiF$_x$ / Al contact was investigated on planar, FZ, n-type (N_d ~ 5×10^{15}cm^{-3}) c-Si wafers coated symmetrically with a LiF$_x$ ~1.5 nm / Al ~15 nm stack. The Al layer is made thick enough to prevent oxidation of the entire layer at the same time as remaining thin enough to allow sufficient light through and not saturate the conductance signal of a photoconductance decay tester (Sinton WCT 120). The lifetime of these samples was too low for this tool to measure accurately, suggesting a high rate of surface recombination. To reduce this rate of surface recombination two candidate passivating layers, suitable for electron-selective heterocontacts when combined with the LiF$_x$ / Al contact. are a-Si:H(i) and TiO$_x$ films. When applied to c-Si both of these films present larger valence band than conduction band offsets potentially assisting in creating a preferential conductivity towards electrons. The Suns-implied V_{oc} behaviour of the two samples are included in Supplementary Figure 3a showing 1 sun implied V_{oc} values of 732 and 695 mV for the wafers coated with a-Si:H(i) and TiO$_x$ films, respectively (Sinton WCT 120). Due to the difference in wafer resistivity, recombination factors (J_0) were extracted using different techniques[7,8] for the a-Si:H(i) and TiO$_x$ coated wafers. Plots of J_0 extractions of wafers coated with a-Si:H(i) and TiO$_x$ layers are included in Supplementary Figure 2b and c, respectively. It should be emphasised that the implied V_{oc} and J_{0c} values represent the recombination before LiF$_x$ / Al deposition and that some changes may occur after contact formation.

Supplementary Note 3. Optimum contact configuration simulations.

Simulations, similar to those in previous studies,[9] are run using the freeware solar cell simulation program *Quokka*.[10] Details of the unit cell characteristics and structure can be

found in Supplementary Table 3. The two variables of the simulation are the rear contact ρ_c and J_{0c}. For every input ρ_c and J_{0c} an optimum rear contact configuration is calculated by means of monitoring the device efficiency. Superimposed experimental data points can be matched with the points of these simulations to provide information on the optimum contact fraction and resultant efficiency which can be achieved. The results of this simulation are shown in Supplementary Figure 4. Experimental optimum ρ_c and J_{0c} data for TiO_x / LiF_x / Al (purple triangle) and a-Si:H(i) / LiF_x / Al (green square) contacts as well as the direct LiF_x / Al (blue circle) contact (a J_0 close to the diffusion limit is assumed[11]) are superimposed on this plot. For the interlayers it can be seen that both contacts are best applied in a 100% contact area and that devices with a-Si:H(i) interlayers have a higher idealised efficiency. It can also be seen that the direct LiF_x / Al contact could be effectively applied in localised contacts (0.5% area) – an architecture which was previously not possible, given the aforementioned difficulties of contacting n-type c-Si.

Supplementary Note 4. Detailed DASH cell characterisation

The champion cell batch consisted of four 2 x 2 cm^2 DASH cells, the light J-V results for these cells have been included in Supplementary Table 2, showing an average cell efficiency for the 4 cells above 19%. The small spread in results seen for each parameter is a testament to the exciting potential of this cell structure.

The champion cell was further characterised by measuring its light J-V behaviour at a range of illumination intensities (see Supplementary Figure 5a) and using the Suns-V_{oc} method (see Supplementary Figure 5b). The V_{oc} values from the three light J-V curves in Supplementary Figure 5a are superimposed on the Suns-V_{oc} curve showing a good correlation between the two methods. No large 'bending' or inflection points are seen in the Suns-V_{oc} curve at high illumination intensities suggesting that there is no large unwanted Schottky barrier affecting the DASH cell.[12] The Suns-V_{oc} data was further used to construct an ideal pseudo J-V plot (see Supplementary Figure 5c) which reflects predicted behaviour of the DASH cell without the effect of parasitic series resistance. From a comparison between the cells pseudo and real J-V curves it can be seen that reducing the series resistance is an obvious path to higher efficiencies. The champion DASH cell light J-V is well fitted using a simple 'one-diode' model (also shown in Supplementary Figure 5c) with a series resistance R_s ~2.09 Ωcm^2. A reduction of R_s to 1 Ωcm^2 (a typical series resistance value for industrial c-Si solar cells) would increase the FF and η to above 79% and 21%, respectively.

The light *J-V* behaviour of the DASH cell was further characterised at a range of temperatures (see Supplementary Figure 5d). From these temperature dependent *J-V* curves an analysis of the V_{oc} and *FF* temperature dependence for the DASH cell was conducted (see Supplementary Figure 5e) and compared to the behaviour of a SHJ cell (taken from Ref.[13]). The SHJ and DASH cells show largely similar behaviour exhibiting the expected decrease in V_{oc} with temperature resulting in coefficients of -1.7 and -2 mV/°C, respectively. Similarly the *FF* evolution with temperature for both the SHJ and DASH cells has a negative gradient with values of -0.04 and -0.06 %/°C, respectively. Such similar temperature dependency of *FF* values suggests that DASH devices perform quite similarly to standard SHJ solar cells in terms of carrier transport.

The light *J-V* performance of a representative DASH cell was also measured before and after a ~10 minute, 100°C anneal without any significant change to the cell performance. This result is important given concerns associated with alkali metal ion incorporation in *c*-Si – centred around both the high mobility of ions and their tendency to form carrier recombination active defect levels within the *c*-Si bandgap.[14] For the latter of these two points Li may be an exception as it has been shown by some authors to form a shallow donor level (even being used as an intentional dopant in some cases[15]). Regardless of this, the stability of the V_{oc} before and after the anneal step suggests that Li incorporation is not an issue at these temperatures. The very high V_{oc} also indicates that the well-known low temperature interaction between Al and *a*-Si:H,[16] is prevented by the thin LiF_x interlayer.

External quantum efficiency (EQE) analysis was also performed on the cells (in-house built set-up) accompanied by front surface reflectance measurements (Lambda 950, Perkin Elmer) to investigate the internal quantum efficiency. An estimation of the J_{sc} is found by integrating the product of the AM 1.5G spectrum (in photons /cm^{-2}nm^{-1}) and the EQE in the 310 – 1200 nm wavelength range. A J_{sc} of 39.4 mA/cm^2 is calculated which, after correcting for a 5% reduction due to the contact fraction, agrees well with the light *J-V* measured value of 37.07 mA/cm^2.

To test the efficacy of the approach on both wafer doping types, simplified cells (1 × 1 cm^2) without passivating interlayers were fabricated on n-type (N_d ~ 5×10^{15} cm^{-3}) and p-type (N_a ~ 7×10^{15} cm^{-3}), planar, FZ wafers. A 15 nm MoO_x hole contact was thermally evaporated on the front-side. This film was capped with a ~60 nm ITO film and a ~1 μm Cu front grid, both of which were sputtered (AJA International, ATC 1800 UHV) at room temperature through two different shadow masks to define the 1 × 1 cm^2 cell area and front grid. The rear contact was formed by evaporating ~1.5 nm of LiF_x followed by ~200 nm of Al without breaking vacuum. The light *J-V* characteristics of these cells was measured under

standard conditions (AM 1.5G spectrum, 100 mW/cm^2, ~25°C) and are provided in Supplementary Figure 5f. The top bus bar was excluded from the cell area for the current density calculation. Both cells exhibit efficiencies in excess of 10%, clearly indicating effective carrier separation. These results demonstrate the effectiveness of the DASH *c*-Si solar cell concept, irrespective of the substrate doping type (similar behaviour is also obtained for conventional doped *a*-Si:H SHJ cells[1]). This highlights a distinction between the DASH cells and the classic metal-insulator-silicon inversion layer (MIS-IL) cell architectures which also avoid the use of doped-silicon layers. The performance of the archetypal p-type MIS-IL cell is strongly linked to both the silicon wafer dopant type and concentration, mainly due to the need to form an Ohmic rear contact.

**Supplementary Table 1** Loss mechanisms associated with doped-silicon.

Limitation	Issue, consequence	Cause	Ref.
Optical	Parasitic free-carrier absorption, reduces J_{sc}	High doping concentration	[17]
	Parasitic window layer absorption, reduces J_{sc}	Using narrow gap window layers (eg. Doped a-Si:H and poly-Si)	[4]
Recombination	Auger and radiative recombination, reduces V_{oc}	High doping concentration	[18]
	SRH recombination, reduces V_{oc}	Dopant precipitates (eg. phosphorus clusters)	[19]
		Dopant complexes (eg. Boron-oxygen defects)	[20]
	Surface SRH recombination, reduces V_{oc}	High surface dopant concentration (currently debated)	[21]
	Bulk and surface recombination, reduces V_{oc}	Band gap narrowing, increased minority carrier concentration	[22]
Transport	Resistive losses, reduces FF (especially lateral R_s)	Dopant and carrier scattering, low majority carrier mobility	[23]
	Low minority carrier diffusion length, reduces J_{sc}	Dopant and carrier scattering, low minority carrier mobility	[23]

**Supplementary Table 2** High efficiency DASH cell results.

	V_{oc} (mV)	J_{sc} (mA/cm^2)	FF	η
Cell1, Champion cell	716.4	37.07	73.15	19.42
Cell 2	716.5	36.97	71.84	19.03
Cell 3	716.7	37.02	71.26	18.91
Cell 4	716.4	37.07	71.1	18.88
Average of 4 cells	716.5	37.03	71.83	19.06

Supplementary Table 3 Assumptions and unit-cell characteristics of simulated cell.

| Symbol	Parameter	Assumption / value
J_{0front}	Front recombination factor	1 fA/cm^2
τ_{bulk}	Bulk lifetime	Richter $et.$ $al.$ intrinsic lifetime[18]
J_g	Generation current density	~44 mA/cm^2
W	Wafer thickness	160 µm
ρ_{bulk}	Bulk type, resistivity	1 Ωcm n-type
J_{0rear}	Rear recombination factor (in non-contacted area)	1 fA/cm^2
m_{frear}	Rear line-contact metal fraction	Finger width = variable, Finger pitch = 1000 µm
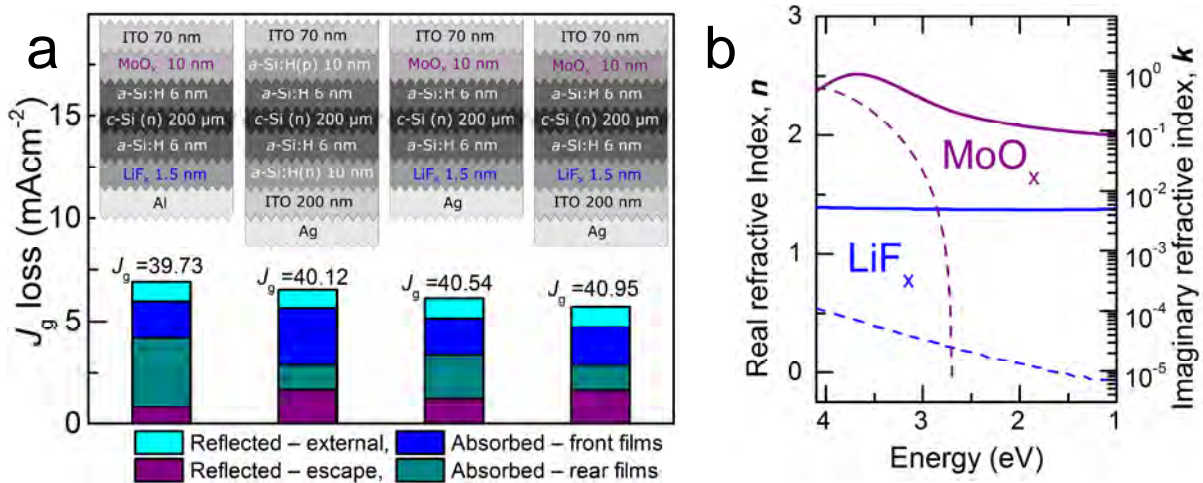
Supplementary Figure 1. Generation current gain analysis. a, Simulations of the loss in generation current for different heterocontact type *c*-Si solar cells. The simulations, conducted using the wafer ray-tracer hosted by *PVlighthouse.com*, assume both surfaces of a 200 µm wafer are random textured and coated with the films as indicated within the figure. The mechanism and location of the current loss in each cell is broken down within each column. b, Measured real (solid) and imaginary (dotted) refractive index values for the MoO_x (purple) and LiF_x (blue) films.
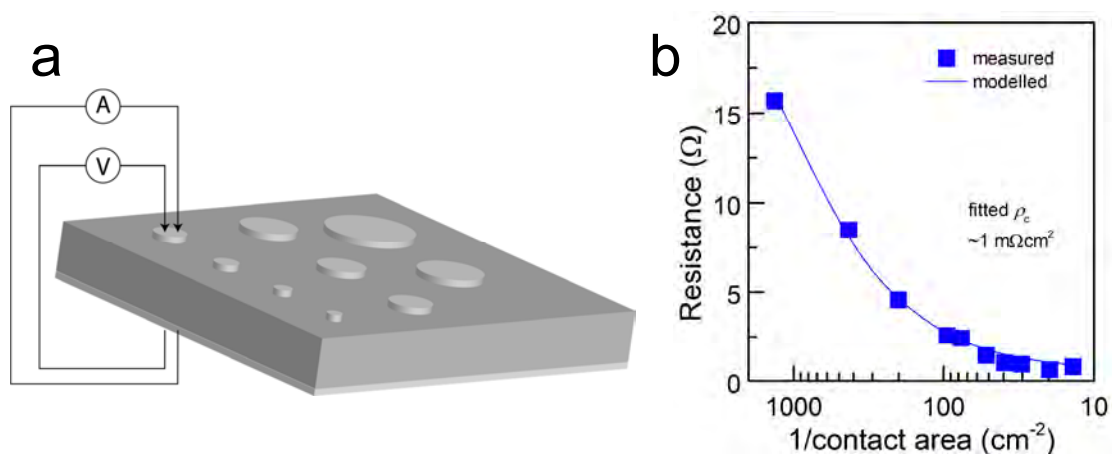
Supplementary Figure 2. Contact resistivity extraction. a, Schematic of the ρ_c test structure. b, Exemplary measured and modelled resistance behaviour of a AMF / Al contact to n-type c-Si.
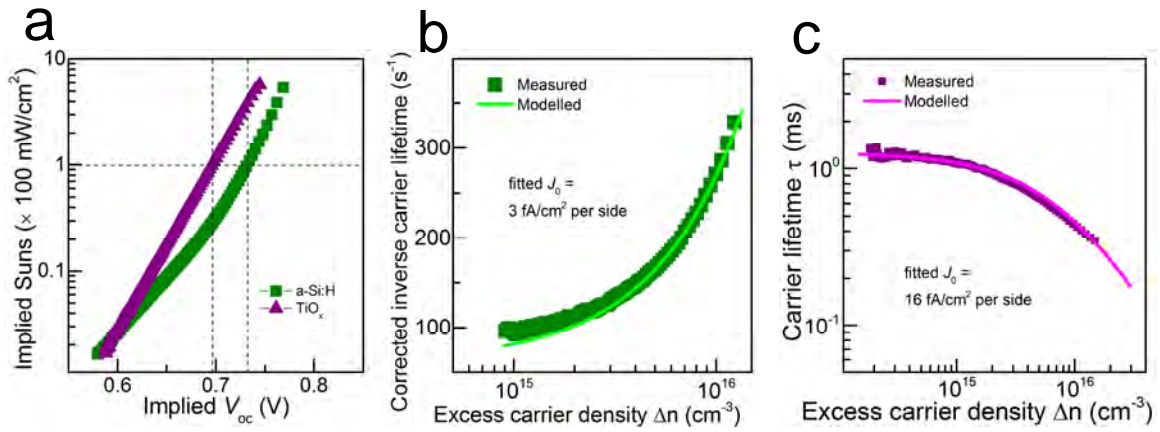
Supplementary Figure 3. a-Si:H and TiO$_x$ interlayer passivation details a, Implied

Suns V_{oc} behaviour for n-type silicon wafers symmetrically passivated with ~6nm of PECVD

a-Si:H(i) or ALD TiO$_x$ films. The dotted horizontal and vertical lines highlight the implied open

circuit voltages at 1 sun. Plots b, and c, show the measured and modelled lifetime behaviour

of n-type wafer coated symmetrically with a-Si:H(i) and TiO$_x$ films, respectively. The models

allow the extraction of surface recombination current pre-factors also provided in the plots.
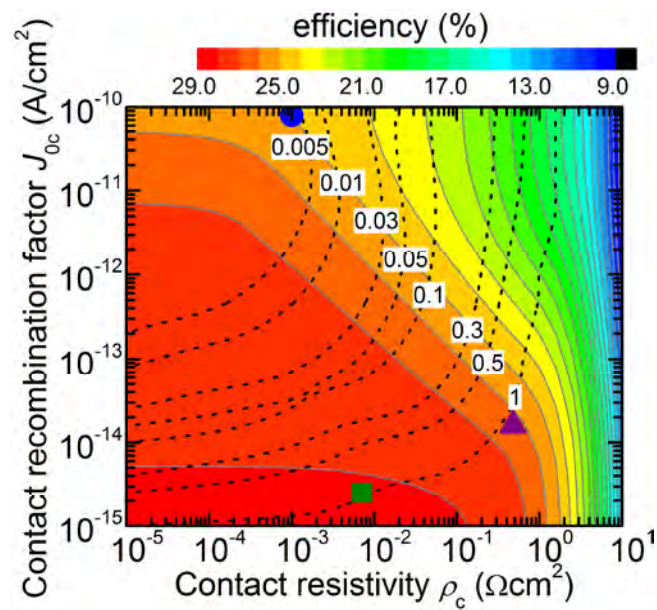
Supplementary Figure 4. Optimum rear contact configuration simulations. *Quokka* simulations of the optimum contact fraction (dotted lines) and resultant idealized efficiency (coloured contours) as a function of the J_{0c} and ρ_c. Values for the direct LiF_x / Al contact (blue circle) as well as the TiO_x / LiF_x / Al (purple triangle) and *a*-Si:H(*i*) / LiF_x / Al contact (green square) are superimposed on the plot.
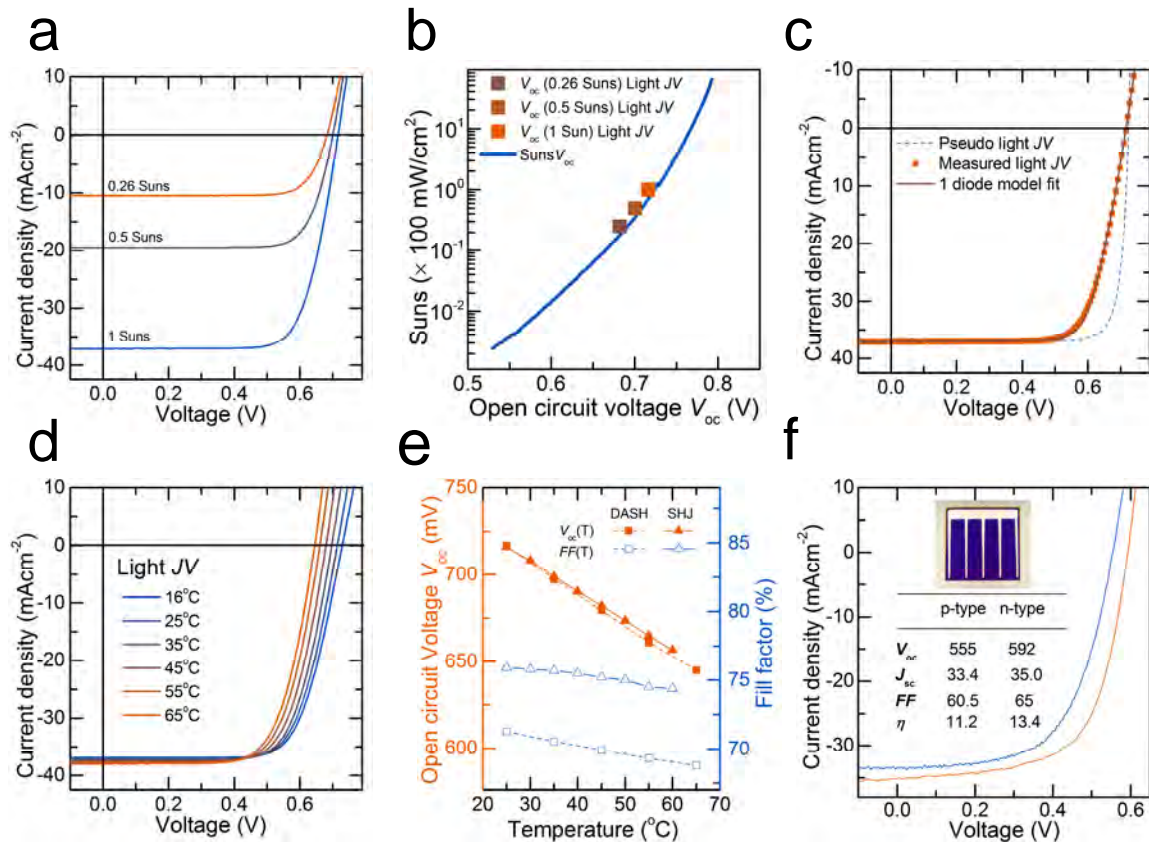
Supplementary Figure 5. Additional solar cell characterisation Light intensity dependent a, J-V and; b, V_{oc} behaviour (from Suns-V_{oc}) of the DASH cell. The Suns-V_{oc} is also used to plot an ideal pseudo J-V curve for the DASH cell in c, which is compared to the real DASH cell light J-V and a simple 'one-diode' fit of the real light J-V data. d, shows the temperature dependent (16 - 65°C) light J-V behaviour of a standard DASH cell measured under 1 sun conditions; and e, compares the voltage and fill factor temperature dependence of DASH and SHJ type cells. f, Light J-V and cell characteristics measured under standard 1 sun conditions of basic n and p-type DASH cells without a-Si:H(i) passivating interlayers showing that effective carrier separation can be achieved regardless of the base wafer doping.

Supplementary References

1. Descoeudres, A. *et al.* >21%; Efficient Silicon Heterojunction Solar Cells on n- and p-Type Wafers Compared. *Photovolt. IEEE J. Of* **3,** 83–89 (2013).

2. Wang, X. J. *et al.* Enhancement of electron injection in organic light-emitting devices using an Ag/LiF cathode. *J. Appl. Phys.* **95,** 3828–3830 (2004).

3. Sakai, J. *et al.* Efficient organic photovoltaic tandem cells with novel transparent conductive oxide interlayer and poly (3-hexylthiophene): Fullerene active layers. *Sol. Energy Mater. Sol. Cells* **94,** 376–380 (2010).

4. Holman, Z. C. *et al.* Current Losses at the Front of Silicon Heterojunction Solar Cells. *Photovolt. IEEE J. Of* **2,** 7–15 (2012).

5. Cox, R. H. & Strack, H. Ohmic contacts for GaAs devices. *Solid-State Electron.* **10,** 1213 – 1218 (1967).

6. Cohen, S. S. Contact resistance and methods for its determination. *Thin Solid Films* **104,** 361 – 379 (1983).

7. D.E. Kane & Swanson, R. M. Measurement of the Emitter Saturation Current by a Contactless Photoconductivity Decay Method. in *Proc of the 18th IEEE Photovoltaic Specialists Conference* 578–583 (1985).

8. Cuevas, A. The effect of emitter recombination on the effective lifetime of silicon wafers. *Sol. Energy Mater. Sol. Cells* **57,** 277 – 290 (1999).

9. Bullock, J. *et al.* Amorphous silicon enhanced metal-insulator-semiconductor contacts for silicon solar cells. *J. Appl. Phys.* **116,** 163706, (2014).

10. Fell, A. A Free and Fast Three-Dimensional/Two-Dimensional Solar Cell Simulator Featuring Conductive Boundary and Quasi-Neutrality Approximations. *Electron Devices IEEE Trans. On* **60,** 733–738 (2013).

11. Mader, C., Muller, J., Eidelloth, S. & Brendel, R. Local rear contacts to silicon solar cells by in-line high-rate evaporation of aluminum. *Sol. Energy Mater. Sol. Cells* **107,** 272 – 282 (2012).

12.   Glunz, S. W., Mackel, H., Nekarda, J. & Cuevas, A. Analyzing back contacts of silicon solar cells by Suns-Voc-measurements at high illumination densities. in *22nd European Photovoltaic Solar Energy Conference and Exhibition* (2007).

13.   Battaglia, C. *et al.* Silicon heterojunction solar cell with passivated hole selective MoOx contact. *Appl. Phys. Lett.* **104,** 113902 (2014).

14.   Chen, J. W. & Milnes, A. G. Energy Levels in Silicon. *Annu. Rev. Mater. Sci.* **10,** 157–228 (1980).

15.   Wysocki, J. J. Lithium-doped radiation resistant silicon solar cells. in *Electron Devices Meeting, 1966 International* **12,** 24–26 (1966).

16.   Bullock, J. *et al.* Amorphous silicon passivated contacts for diffused junction silicon solar cells. *J. Appl. Phys.* **115,** 163703, (2014).

17.   Baker-Finch, S. C., McIntosh, K. R., Yan, D., Fong, K. C. & Kho, T. C. Near-infrared free carrier absorption in heavily doped silicon. *J. Appl. Phys.* **116,** 063106, (2014).

18.   Richter, A., Glunz, S. W., Werner, F., Schmidt, J. & Cuevas, A. Improved quantitative description of Auger recombination in crystalline silicon. *Phys. Rev. B* **86,** 165202 (2012).

19.   Min, B. *et al.* Heavily doped Si:P emitters of crystalline Si solar cells: recombination due to phosphorus precipitation. *Phys. Status Solidi RRL Rapid Res. Lett.* **8,** 680–684 (2014).

20.   Schmidt, J. & Cuevas, A. Electronic properties of light-induced recombination centers in boron-doped Czochralski silicon. *J. Appl. Phys.* **86,** 3175–3180 (1999).

21.   King, R. R., Sinton, R. A. & Swanson, R. M. Studies of diffused phosphorus emitters: saturation current, surface recombination velocity, and quantum efficiency. *Electron Devices IEEE Trans. On* **37,** 365–371 (1990).

22.   Yan, D. & Cuevas, A. Empirical determination of the energy band gap narrowing in p+ silicon heavily doped with boron. *J. Appl. Phys.* **116,** 194505, (2014).

23.   Klaassen, D. B. M. A unified mobility model for device simulation: Model equations and concentration dependence. *Solid-State Electron.* **35,** 953 – 959 (1992).